using a combination of high-density (closely spaced) expendable bathythermograph (XBT) and broader-scale Argo profiling float data (Dong et al. 2014, not shown; www.aoml.noaa.gov/phod/soto/mht/ax18/report.php). These data are collected and analyzed in near-real time, with values spanning July 2002 to September 2017.

Similar to 26°N, at 41°N the AMOC and AMHT are decreasing less rapidly (Fig. 3.23), changing to −0.08 (±2.7) Sv decade^{-1} and −0.03 (±0.04) PW decade^{-1} as compared with −1.2 (±3.0) Sv decade^{-1} and −0.09 (±0.21) PW decade^{-1} reported last year. Farther south, the MOC/MHT trends are positive, but decreasing in the past three years as the annual means at 16°N increased from −29.2 Sv in 2014 to −27.8 Sv in 2015 to −23.8 in 2016. This recent reduction in southward flow has led to a reduced estimate of the long-term trend of the AMOC from February 2000 to September 2016 at 16°N to be +3.4 (±2.4) Sv decade^{-1}. While the 35°S AMOC transport estimate has remained fairly constant for the last three years (median AMOC of about 20 Sv), during 2017 it was dominated by the Ekman component whereas in previous years it had been dominated by the geostrophic component. The variability at all latitudes in the Atlantic is not well correlated and, therefore, data from more than one latitude are needed to describe the state of the ocean.

i. Global ocean phytoplankton—B. A. Franz, E. M. Karaköylü1, D. A. Siegel, and T. K. Westberry

Marine phytoplankton contribute roughly half the net primary production (NPP) on Earth, fixing atmospheric CO_2 into food that fuels global ocean ecosystems and drives biogeochemical cycles (e.g., Field et al. 1998; Falkowski et al. 1998). Phytoplankton growth is dependent on availability of light and nutrients (e.g., iron, nitrogen, phosphorous) in the upper ocean euphotic zone, which in turn is influenced by physical factors such as ocean temperature (e.g., Behrenfeld et al. 2006). SeaWiFS (McClain 2009) and MODIS (Esaias et al. 1998) are satellite ocean color sensors that provide observations of sufficient frequency and geographic coverage to globally monitor changes in the near-surface concentration of the phytoplankton pigment chlorophyll-*a* (Chl*a*; mg m^{-3}), which serves as a proxy for phytoplankton abundance. Here, global Chl*a* distributions for 2017 are evaluated within the context of the 20-year continuous record provided through the combined observations of SeaWiFS (1997–2010) and MODIS on *Aqua* (MODISA, 2002–present). All Chl*a* data used in this analysis correspond to NASA process-

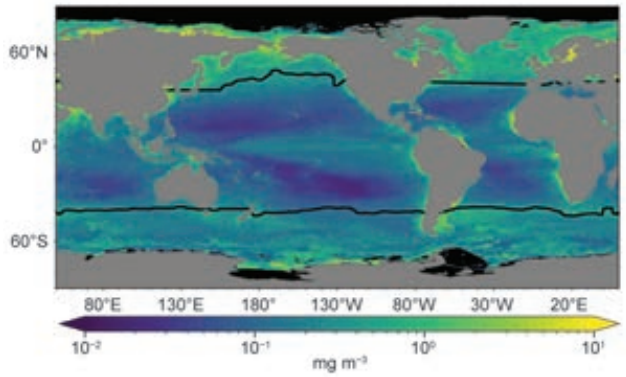

Fig. 3.24. Annual mean Chl*a* distribution mg m^{-3} derived from MODIS on *Aqua* for 2017. Also shown is the location of the mean 15°C SST isotherm (black lines) delineating the boundary of the PSO. Chl*a* data are from NASA Reprocessing version 2018.0. Data are averaged into geo-referenced equal area bins of approximately 4.6 × 4.6 km^2 and mapped to an equirectangular projection centered at 150°W.

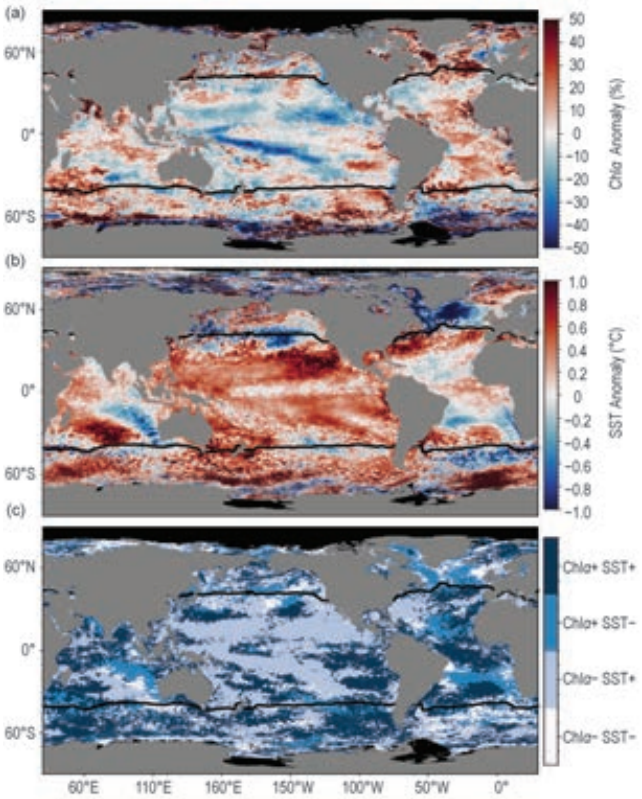

Fig. 3.25. Spatial distribution of average monthly (a) MODISA Chl*a* anomalies and (b) SST anomalies where monthly differences were derived relative to the MODISA 9-year climatological record (2003–11). Chl*a* is expressed as % difference from climatology, while SST is shown as an absolute difference (°C). (c) identifies relationships between the sign of SST and Chl*a* anomalies from panels (a) and (b), with colors differentiating sign pairs and missing data masked in black. Also shown in each panel is the location of the mean 15°C SST isotherm (black lines) delineating the PSO.

ing version R2018.0 (https://oceancolor.gsfc.nasa.gov/reprocessing/), which utilizes common algorithms and calibration methods to maximize consistency in the multi-mission satellite record.

The spatial distribution of MODISA annual mean Chl*a* for 2017 (Fig. 3.24) is consistent with the well-established, physically driven distribution of nutrients (Siegel et al. 2013) and surface mixed-layer light conditions (Behrenfeld et al. 2016). Chl*a* values during 2017 ranged over three orders of magnitude, from < 0.02 mg m^{-3} in the central ocean gyres to > 20 mg m^{-3} in nutrient-rich coastal and subpolar waters. To assess changes in this distribution during 2017, mean values for MODISA Chl*a* in each month of the year were subtracted from monthly climatological means for MODISA (2003–11). These monthly fields were then averaged to produce the global chlorophyll anomaly map for 2017 (Fig. 3.25a). Identical calculations were performed on MODISA sea surface temperature (°C) data to produce an equivalent SST annual mean anomaly (Fig. 3.25b), used to illustrate the relationships between Chl*a* and SST anomalies (Fig. 3.25c). Here the permanently stratified ocean (PSO) is defined as the region where annual average surface temperatures are > 15°C (black lines in Figs. 3.24 and 3.25) and is characterized by surface mixed layers that are typically low in nutrients and shallower than the nutricline (Behrenfeld et al. 2006).

Consistent with the establishment of weak La Niña conditions through much of 2017, Chl*a* concentrations along the equatorial Pacific were neutral to slightly elevated (<10%) above the climatological mean (Fig. 3.25a), reflecting the return of cooler, more nutrient-rich waters conducive to phytoplankton growth. Chl*a* concentrations throughout much of the tropical Pacific, however, were generally diminished relative to climatological values (10%–30%) and inversely related to SST anomalies (gray areas above and below the equator in Fig. 3.25c). Annual mean SST anomalies (Fig. 3.25b) generally coincide with surface mixed layer depth (MLD) anomalies in the PSO, with warmer temperatures associated with shallower mixing, such that phytoplankton spend more time near the ocean's surface and thus have higher daily sunlight exposures than deeper mixing populations. Phytoplankton respond to this increased light by decreasing their cellular chlorophyll levels (Behrenfeld et al. 2016). A secondary consequence of decreased MLD is a decrease in the vertical transport of nutrients to the surface layer, but coupling between the MLD and nutricline depths throughout much of the PSO is known to be weak (Lozier et al. 2011). Modestly depressed Chl*a* concentrations (< 10%) were also observed throughout the Sargasso Sea and in the Mediterranean in 2017. Strongly elevated Chl*a* concentrations were observed in the northern reaches of the North Atlantic (>30%), with weaker increases observed throughout much of the South Atlantic and Indian Ocean regions. Within the boundaries of the PSO, an inverse relationship was generally observed between Chl*a* and SST anomalies (light blue and gray colors in Fig. 3.25c), with some notable exceptions of positive correlations between Chl*a* and SST anomalies in the South Atlantic and southwestern Pacific (dark blue colors in Fig. 3.25c). In regions outside the PSO, no clear relationship was observed between Chl*a* and SST anomalies (Fig. 3.25c), consistent with previous studies (e.g., Behrenfeld et al. 2006; Franz et al. 2017).

Over the 20-year time series of spatially integrated monthly mean Chl*a* values for the PSO (Fig. 3.26a) mean concentrations varied by ~20% (±0.03 mg m^{-3}) around a long-term average of ~0.14 mg m^{-3}. This variability includes significant seasonal cycles in

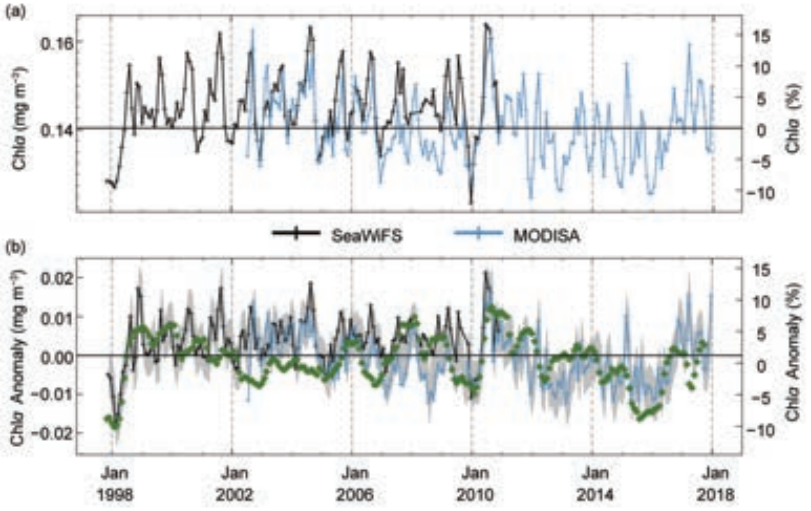

Fig. 3.26. 1998–2017, multimission record of Chl*a* averaged over the PSO for SeaWiFS (black) and MODISA (blue). (a) Independent record from each mission, with horizontal black line indicating the multimission mean Chl*a* concentration for the region (mg m^{-3}). (b) Monthly anomaly (%) for SeaWiFS and MODISA after subtraction of the 9-year MODISA monthly climatological mean (2003–11) from each mission record. The gray region in (b) shows the averaged difference between SeaWiFS and MODISA over the common mission lifetime. Green diamonds show the MEI, inverted and scaled to match the range of the Chl*a* anomalies.

Chl*a* distributions and responses to climatic events. The time series also demonstrates the high level of consistency between the overlapping periods of the SeaWiFS and MODISA missions, lending confidence to interpretation of the multimission record.

Chl*a* monthly anomalies within the PSO (Fig. 3.26b) show variations of ±15% (±0.02 mg m^{-3}) over the multimission time series. For 2017, these anomalies were relatively constant and slightly elevated (+0.005 mg m^{-3}, on average) relative to the long-term mean, consistent with the weak La Niña conditions as discussed previously. The link between ENSO variability and mean Chl*a* response in the PSO is demonstrated by the correspondence of anomaly trends with the multivariate ENSO index (MEI; Wolter and Timlin 1998; Fig. 3.26b, green diamonds, presented in the inverse to illustrate the covariation). From 1997 through 2017, monthly anomalies in Chl*a* concentration within the PSO continue to track large-scale climate oscillations as captured by the MEI (Fig. 3.26b), with some notable deviations in the 2002–06 period.

Variability and trends in Chl*a* reflect both adjustments in phytoplankton biomass and physiology (or health). Both of these properties are mechanistically linked to physical properties of the upper ocean, as well as ecological relationships between phytoplankton and their zooplankton predators. Unraveling the diversity and covariation of factors that influence Chl*a* concentrations is essential for correctly interpreting the implications of Chl*a* anomalies on ocean biogeochemistry and food webs. For example, inverse relationships between Chl*a* and SST can emerge from changes in either mixed-layer light levels or vertical nutrient flux, but these two mechanisms have opposite implications on phytoplankton NPP (Behrenfeld et al. 2016). An additional complication is that measured changes in ocean color often contain a contribution from colored dissolved organic matter (Siegel et al. 2005) that can be mistakenly attributed to changes in Chl*a* (Siegel et al. 2013). Thus, while the satellite record of ocean color continues to provide critical insights on global processes, ongoing effort and new approaches are needed to fully understand the story these data are telling regarding relationships between climate and marine ecosystems.

j. Global ocean carbon cycle—R. A. Feely, R. Wanninkhof, B. R. Carter, P. Landschützer, A. Sutton, and J. A. Triñanes

As a consequence of humankind's collective release of CO_2 emissions into the atmosphere from fossil fuel burning, cement production, and land use changes over the last 250 years, referred to as Anthropogenic CO_2 (C_{anth}), the atmospheric CO_2 has risen from pre-industrial levels of about 278 ppm (parts per million) to about 405 ppm (see Section 2g1). The atmospheric concentration of CO_2 is now higher than has been observed on Earth for at least the last 800 000 years (Lüthi et al. 2008). As discussed in previous *State of the Climate* reports, the global ocean is a major sink for C_{anth}. Here the discussion is updated to include recent estimates of that sink. Over the last decade the global ocean has continued to take up a substantial fraction of the anthropogenic carbon (C_{anth}) emissions and therefore is a major mediator of global climate change. Of the 10.7 (±0.9) Pg C yr^{-1} C_{anth} released during the period 2007–16, about 2.4 (±0.5) Pg C yr^{-1} (26%) accumulated in the ocean, 3.0 (±0.8) Pg C yr^{-1} (30%) accumulated on land, and 4.7 (±0.1) Pg C yr^{-1} (43%) remained in the atmosphere with an imbalance of 0.6 Pg C yr^{-1} (Le Quéré et al. 2018). This decadal ocean carbon uptake estimate is a consensus view based on a combination of measured decadal inventory changes, models, and global air–sea CO_2 flux estimates based on surface ocean partial pressure of CO_2 (pCO_2) measurements. Using ocean general circulation models that include biogeochemical parameterizations (OBGCMs) and inverse models that are validated with observations-based air–sea exchange fluxes and basin-scale ocean inventories, Le Quéré et al. (2018) have demonstrated that the oceanic anthropogenic carbon sink has grown from 1.0 (±0.5) Pg C yr^{-1} in the decade of the 1960s to 2.6 (±0.5) Pg C yr^{-1} in 2016. Air–sea CO_2 flux studies reported here indicate an ocean uptake of C_{anth} of 2.6 Pg C yr^{-1} for 2017.

1) Air–sea carbon dioxide fluxes

Ocean uptake of C_{anth} can be estimated from the net air–sea CO_2 flux derived from the bulk flux formula with air–sea differences in CO_2 partial pressure (ΔpCO_2) and gas transfer coefficients as input. A steady contribution of carbon from riverine runoff, originating from organic and inorganic detritus from land, estimated at 0.45 Pg C yr^{-1} (Jacobson et al. 2007) is included to obtain the C_{anth} uptake by the ocean. The data sources for pCO_2 are annual updates of surface water pCO_2 observations from the Surface Ocean CO_2 Atlas (SOCAT) composed of mooring and ship-based observations (Bakker et al. 2016) and the LDEO database with ship-based observations (Takahashi et al. 2018). The increased observations and improved mapping techniques such as neural network methods and self-organizing maps (Landschützer et al. 2013, 2014; Rödenbeck et al. 2015) provide global pCO_2 fields on a 1° latitude × 1° longitude grid at monthly time scales annually. This allows investigation of